CHEMIJA. 2015. Vol. 26. No. 1. P. 9–17

Corrosion resistance of Mg-Nb alloy films in Hank's balanced salt solution

Asta Grigucevičienė*,

Konstantinas Leinartas,

Laurynas Staišiūnas,

Povilas Miečinskas,

Vitalija Jasulaitienė,

Jūratė Vaičiūnienė,

Eimutis Juzeliūnas

Center for Physical Sciences and Technology, A. Goštauto St. 9, LT-01108 Vilnius, Lithuania

Magnesium alloys are promising materials for in vivo applications due to superior mechanical properties, biodegradability and biocompatibility. Novel Mg-*x*Nb systems with Nb content ranging between 4 and 44 at.% were formed by sputtering technique. Electrochemical and corrosion behaviour of the alloys was studied in Hank's balanced salt solution employing the methods of inductively coupled plasma / optical emission analysis, DC voltammetry, electrochemical impedance spectroscopy (EIS) and X-ray photoelectron spectroscopy (XPS). The experiments showed ennoblement of the alloys with increase in Nb concentration. High corrosion resistance was achieved when Nb content in the alloy exceeded ~26 at.%. EIS data indicated the presence of two oxygen containing layers on the corroding surface: a thin and highly protective one next to the metal, and much thicker, but porous and poorly protective layer on the top. It has been concluded that corrosion reactions occur predominantly within the pores of the thin protective layer composed of MgO+NbO. By changing Nb content the corrosion rate of Mg-Nb alloys could be adjusted according to biomedical in vivo requirements.

Key words: Mg-Nb alloy, magnetron sputtering, Hank's solution, voltammetry, EIS

INTRODUCTION

Magnesium-niobium composite systems have recently attracted an interest as promising materials for hydrogen storage devices [1–9], optically switchable mirrors [10, 11] and biomedical applications in vivo [12]. Mg-Nb composites integrate such beneficial properties as high corrosion resistance of Nb and lightness of Mg. Although the first co-deposition of Mg-Nb has been reported about two decades ago [13], studies of this subject have only recently gained momentum, the driving force of which is the possibility to use these systems in the above fields of application.

Magnesium, due to its intrinsic electronegativity, is very susceptible to corrosion. This limits application of this valuable lightweight metal in numerous technical fields where lightness of materials is of importance: portable electronics, computers or aircraft and automotive industry. To the contrary, in biomedical applications, high corrosion activity of magnesium is a desirable property, which enables dissolution of implants in vivo, so that there is no need for secondary surgery to remove temporary implants such as those for osteosynthesis, cardiovascular stents or tissue scaffolds [14–41].

In terms of in vivo applications, magnesium-based alloys have superior mechanical properties, which are similar to those of bones. Magnesium alloys outperform such permanent materials as Ti, stainless steel or Co-Cr alloy [21, 24, 25]. Another important property of magnesium is its excellent biocompatibility. Mg^{2+} ions are the most common ions in the human body after Na^{+}, Ca^{2+} and K^{+}. Magnesium is an essential element in human bones as well as in muscles or soft tissues. Mg^{2+} is known as a stabilizer of DNA and RNA structures. These ions are of importance for metabolic enzymes, their deficiency causes dysfunction of cell membranes and increases incidence of cancer and heart diseases. It is also important that a toxic dose of magnesium is unknown and cytotoxic activity of Mg^{2+} released from Mg on osteoblast cells was not determined [24]. On the contrary, it has been found that magnesium in damaged locus promotes bone growth [14, 21].

The corrosion rate of an implant has to be adjusted according to medical needs. For instance, in the case of stents, appreciable degradation should start after about 6 months, which is followed by the vessel reconstruction period completed within the next 6 months [19]. Therefore, the total degradation of the implant during the period of 12 to 24 months is desired [19, 26]. It is important to adjust the degradation rate so that to avoid an intolerable accumulation of the degradation products such as hydrogen or alloying components.

* Corresponding author. E-mail: asta@chi.lt

Alloying and tailoring the composition is an effective approach to control the corrosion behavior of Mg alloys in vivo. However, the main issues in this case are biocompatibility and toxicity of the modified surfaces and the alloying additives. For instance, Al, Zn and Mn may cause harmful effects such as dementia (Al), neurotoxicity leading to Parkinsonism (Mn) and liver, lung, breast or nasopharyngeal cancer (Zr) [29, 37, 40–43].

In this study Nb was used as a possible alloying additive for decreasing of Mg corrosion. Nb is a valve metal, which readily forms protective surface oxide and, therefore, has excellent corrosion resistance in most aqueous environments. Nb neither dissolves in Mg matrix nor forms intermetallic phases with it [44, 45]. Nb is known to be non-toxic and physiologically inert. Nb treated with hydroxide forms a bonelike oxide layer that helps osteointegration [46, 47].

There is quite a few information about corrosion performance and electrochemical behaviour of Mg-Nb alloys. Here we studied corrosion behaviour of Mg-Nb alloys in a wide range of Nb concentrations in Hank's balanced salt solution (BSS), which has physiological pH and salt concentrations.

EXPERIMENTAL

Magnetron sputtering of Mg and Nb targets was performed using a Univex 350 vacuum system from Leybold Vacuum GmbH (Germany) equipped with two confocal DC magnetrons. The sputtering chamber was evacuated up to ~2.2×10^{-6} mbar and then filled with working gas (Ar), maintaining the gas pressure at 1.6×10^{-3} mbar. Targets were prepared from pure Mg (99.9%) and Nb (99.9%), both from Alfa Aesar GmbH (Germany). Glass discs of 14 mm in diameter were used as substrates, the temperature of which was kept at ~60 °C by an integrated infrared heater. The sputtering power was from 95 to 110 W for Mg and from 5 to 90 W for Nb. A holder with the substrates was rotated at a velocity of 13 rpm to ensure uniform coating distribution. The Mg/Nb concentration ratio in the deposits was changed by varying sputtering power of the magnetrons. Thickness of the films of Mg-*x*Nb alloys was ca. 400 to 500 nm.

Composition of Mg-Nb alloys was determined by a microprobe of a scanning electron microscope (SEM) EVO-50EP from Carl Zeiss SMT AG (Germany) equipped with a secondary electron detector. Compositions of the alloys throughout the paper are given in atomic %, e. g. Mg-4Nb.

The surface composition of the as-formed alloys and those after immersion in Hank's solution was studied by X-ray photoelectron spectroscopy (XPS). The data were recorded by a VG Escalab MK II spectrometer from VG Scientific (UK) using X-radiation of MgKα anode (energy of 1 253.6 eV, constant pass energy of 20 eV). The pressure in the UHV analyser chamber was maintained at 1.33×10^{-7} Pa during measurements. Concentrations of elements were calculated from the intensity of the lines Mg 2p, Nb 3d, O 1s, P 2p and Ca 2p. The surface spectra for every element were recorded 3–5 times and the data obtained were averaged and compared with the standards [48]. For determination of depth profiles the samples were etched by beam of Ar^+ ions of 3 kV power at a vacuum of 5×10^{-4} Pa. Beam currents of 20 μA cm^{-2} were used.

Mg(II) and Nb(V) concentrations in Hank's solutions before and after the exposure of Mg-*x*Nb alloys were determined by inductively coupled plasma / optical emission spectrometry (ICP/OES). A spectrometer "Optima 7000DV" from Perkin Elmer (USA) was calibrated by using standard solutions of 1.00 and 10.00 mg/l. Metals concentrations were determined at the wavelengths: λ_{Mg}285.213 and 280.271 nm; λ(Nb) = 309.418 and 269.706 nm. The correlation coefficients were: λ_{Mg}285.213 nm = 0.999994; λ_{Mg}280.271 nm = 0.999993, λ_{Nb}309.418 nm = 0.999993; λ_{Nb}269.706 nm = 0.999991.

Voltammetric and electrochemical impedance spectroscopy (EIS) measurements were carried out using the electrochemical measurement system Parstat2273 from Princeton Applied Research (USA). Measurements were performed at 20 ± 1 °C in a naturally aerated Hank's Balanced Salt Solution (HBSS) from Sigma Aldrich (Germany). The composition of Hank's solution was the following (g/l): 0.185 $CaCl_2 \times 2H_20$, 0.097 $MgSO_4$, 0.4 KCl, 0.06 KH_2PO_4, 0.35 $NaHCO_3$, 8.0 NaCl, 0.048 Na_2HPO_4, 1.0 glucose and 0.011 Phenol Red, pH 7.2–7.6. Phenol Red is used for visual control of HBSS pH. Ag/AgCl (in saturated KCl) was used as a reference electrode and all potential values are referred to this electrode. Platinum plate of ~4 cm^2 area was used as a counter electrode. The working electrode (glass disc with deposited Mg-*x*Nb alloy) was mounted in a special holder and placed into a three-electrode electrochemical glass cell. The area of the working electrode surface exposed to the electrolyte was 0.5 cm^2. Stationary polarization curves were recorded under potentiodynamic mode at the potential scan rate of 0.5 mV/s. EIS spectra were recorded under the open circuit potential in a potentiostatic mode with the potential amplitude of ±5 mV. The frequency range from 20 kHz to 0.1 Hz was employed, which permitted to perform a single scan in less than 1 min. Electrochemical measurements started after 3–5 min of electrode exposure to the HBSS solution. This period was used to allow the sample to equilibrate with the medium before the scan began. EIS data analysis and simulation were performed using the authorized ZSimpWin™ software.

RESULTS AND DISCUSSION

Mg-*x*Nb alloys with Nb concentrations ranging from 4 to 44 at.% were deposited on glass substrates. X-ray diffraction measurements indicated substitutional solid solutions of Nb in the *hcp* Mg lattice for Nb concentrations from 4 to 26 at.% [49]. At higher Nb content (32 and 44 at.% of Nb) formation of a solid solution of Mg in the *bcc* Nb lattice was determined. The increase of Nb concentration in Mg alloys induced the effects of *hcp* lattice contraction and

a simultaneous refining of the coating grains from ~144 nm for pure Mg to ~90 and ~34 nm for Mg-4Nb and Mg-9Nb alloys, respectively. The alloys with higher Nb content were composed of crystallites of ~30 nm size.

The results of analytical investigations of the concentration of Mg^{2+} ions found in the Hank's solution after exposure of the Mg-Nb systems are summarized in Fig. 1. These data characterize corrosion resistance of the sputtered films. Evidently, the dissolution (corrosion) rate decreases with an increase in Nb concentration. A substantial increase in the concentration of Mg^{2+} ions was determined for the Mg-4Nb, Mg-9Nb and Mg-14Nb, while at higher Nb content only negligible increase was found. One can conclude that the systems with 26 to 44 at.% of Nb are rather stable in the solution investigated. Niobium ions were not detected in the solution prior and after corosion of any investigated alloys. The obtained data clearly show that the corrosion rate of Mg-Nb films may be tuned to a desirable rate by changing Nb concentration. This result is of practical importance for in vivo applications.

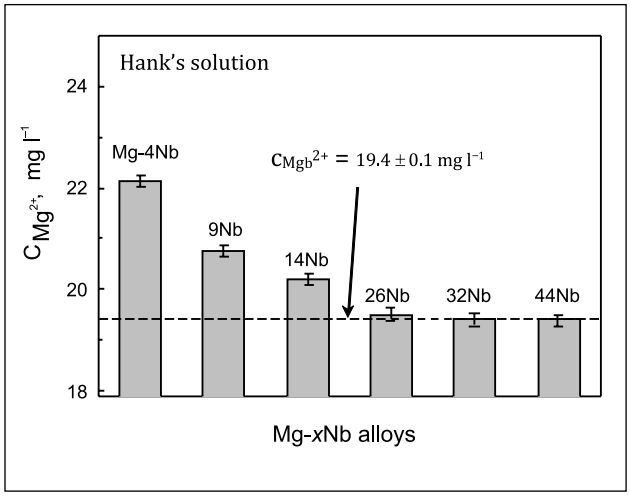

Fig. 1. Change of bulk concentration of Mg^{2+} ions in Hank's solution after 10 min exposure of Mg-xNb alloys. Dashed line shows Mg^{2+} concentration in Hank's solution before immersion

Corrosion resistance was also characterized by the measurements of the open circuit potential (E_{ocp}) and anodic activity (Fig. 2). Figure 2 shows the E_{ocp} change from <~ –1.45 V for pure Mg to ~–1.07 V for Mg-44Nb (curves 1 and 7, respectively). The positive shift of E_{ocp} implies a substantial increase in samples stability in the solution. An ennoblement of the system with an increase in the Nb concentration is evident also from the positive shift of the polarization curves along with appearance of some passive regions. Limiting passive currents followed by breakdown potentials (E_{bd}) appear when sweeping the potential from E_{ocp} for the samples with Nb concentration 26% or more (curves 5 to 7 in Fig. 2). This shows substantially reduced electrochemical activity of these samples.

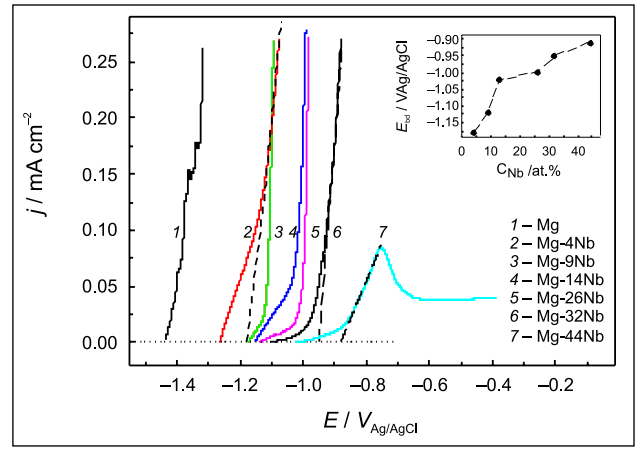

Fig. 2. Anodic polarization curves of Mg-*x*Nb alloys in Hank's solution. Insert: dependence of E_{bd} on Nb content in alloy. $v = 0.5$ mv/s

The parameters of the corrosion process were also evaluated by EIS. The measured and the fitted impedance spectra of alloys as the function of exposure time are presented in Nyquist plots in Figs. 3a and 3b. The measurements in the low frequencies domain were limited by 100 mHz. Reduction of frequencies led to great data scattering, most probably, due to significant changes in surface properties. Also, at prolonged exposures, there is a risk of complete or partial dissolution of the thin films.

Figure 3a shows the EIS spectrum of Mg-4Nb alloy after 5 min exposure (curve 1). It has a well-defined semicircle capacitive loop (a time constant) in the medium-frequency range ~(12.9 kHz to 1 Hz) and a less defined inductive loop in the low-frequency range, that is below 1.0 Hz. Both the real and the imaginary parts of impedance increase during the exposure and at the same time the shift of the semicircle center along x-axis is observed. Such evolution of the spectrum shape is indicative of total impedance increase and decrease in electrical capacitance with the exposure time. The increase in the impedance value implies the increased retarding of the charge transfer rate and, in turn, the inhibition of the corrosion process, which occurs according to the partial charge transfer reactions as follows:

$$Mg \rightarrow Mg^{2+} + 2e^{-}, \quad (1)$$

$$Nb \rightarrow Nb^{2+} + 2e^{-}, \quad (2)$$

$$2H_2O + 2e^{-} \rightarrow H_2 + 2OH^{-}. \quad (3)$$

A decrease in the double layer capacitance is attributable to the thicknening of the surface layer due to accumulation of corrosion products on the sample surface (capacitance inversely proportional to the thickness of the double layer). Thickening of the corrosion product layer occurs according to the chemical reaction of precipitation:

$$Mg^{2+} + 2OH^{-} \rightarrow Mg(OH)_2. \quad (4)$$

Comparison of the Nyquists diagrams for all studied alloys after 1 h exposure clearly shows that the increase in the Nb content led to the increase in the total electrode impedance (Fig. 3c). An exception was only observed for the Mg-26Nb alloy, the impedance of which was higher than that of Mg-32Nb. Such behavior may be explained by the change of the crystal lattice from *hcp* to *bcc* occurring in this range of Nb concentration [49].

According to the literature data on Mg corrosion in neutral media [52], the interface and charge transfer are modeled as follows: (i) a thin protective layer composed of MgO-NbO is formed progressively at the metal-solution interface; (ii) this layer has some porosity and the reactions of Mg and Nb dissolution (1) and (2) take place inside the pores at the Me-solution boundary; (iii) a thick and poorly protective layer of $Mg(OH)_2$ forms on the top of the thin MgO-NbO film according to the reaction (4) as well as the reaction of magnesium oxide with water:

$$MgO + H_2O \rightarrow Mg(OH)_2. \quad (5)$$

According to Pourbaix diagrams [50], niobium in neutral media is present in the form of an oxide. During corrosion this oxide is incorporated into the surface structure and forms a $Mg(OH)_2$ + NbO layer with better protective capabilities compared to those of the single $Mg(OH)_2$. XPS studies confirmed such assumption (Fig. 4). Evidently, Nb is present within the entire outermost surface layer (10 nm). It is also important that the concentration ratio Nb/Mg in the corrosion products layer is higher than that in the alloy. For instance, more or less equal quantities of both components were determined within the oxygen containing a surface layer in the alloy with only 14% of Nb (Fig. 4a). Moreover, about three times higher Nb concentration compared to that of Mg was found within the surface layer in the case of alloy with 44% of Nb.

The measured impedance data were analyzed on the basis of the Kramers-Kronig (KK) relationship using the ZsimpWin software. Evaluation of impedance spectra by the

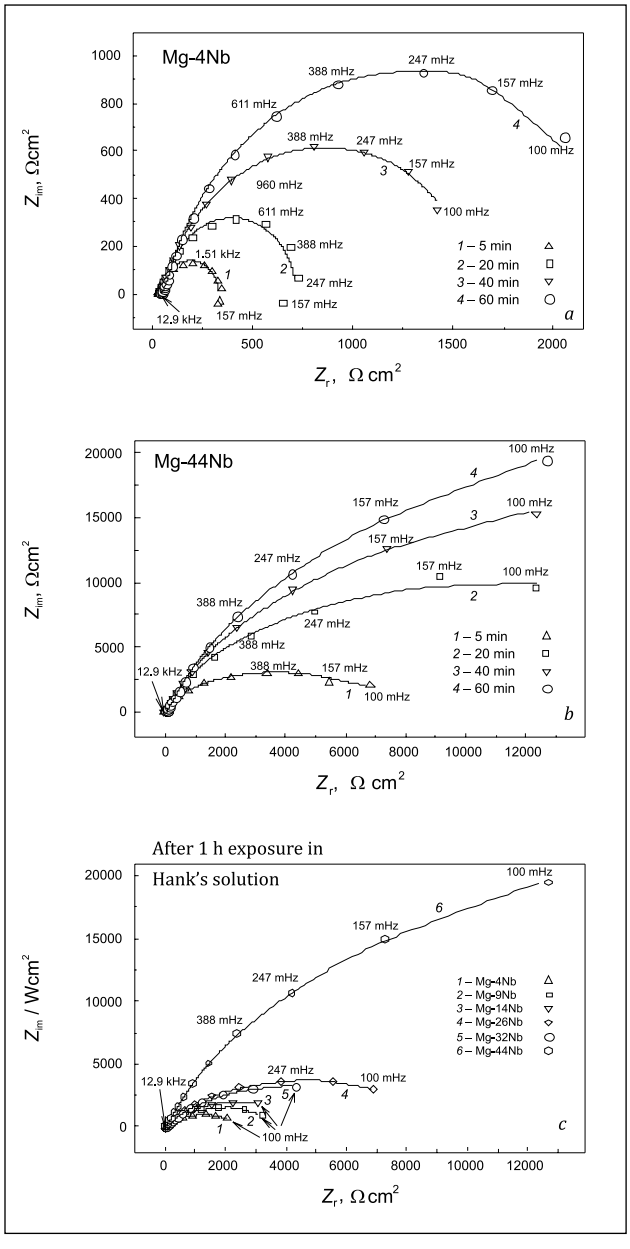

Fig. 3. Dependences of Z_{im} (imaginary) and Z_r (real) impedances of Mg-4Nb (*a*) and Mg-44Nb (*b*) electrodes on exposure time in Hank's solutions. *c* shows the Nyquist diagram of Mg-*x*Nb electrodes after 1 h exposure

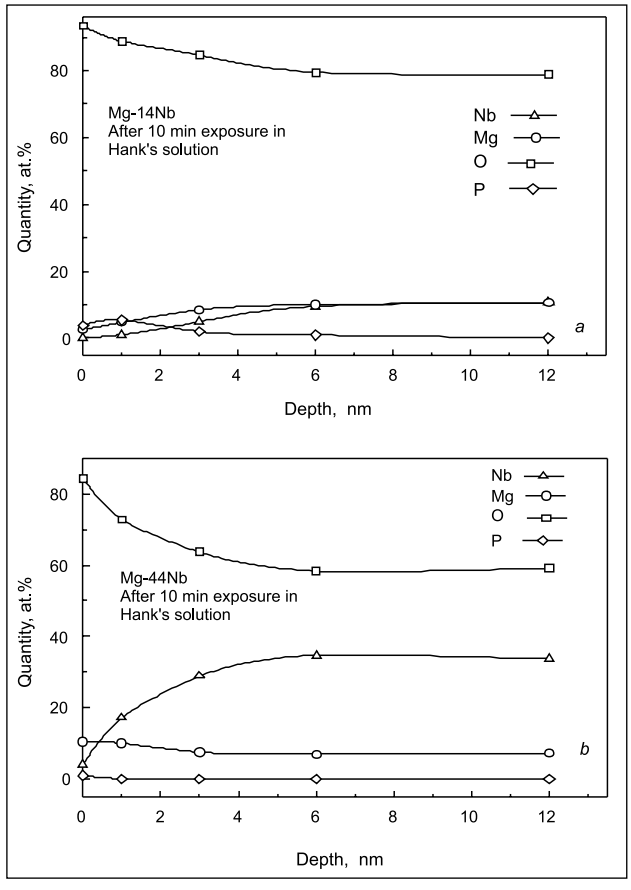

Fig. 4. Concentration depth profiles of Mg-14Nb (*a*) and Mg-44Nb (b) surface after 10 min exposure in Hank's solution

Voigt measurement model [51] showed that the number of time constants for the EIS spectra was 3. For the electrodes with Nb content ranging between 9 and 32 at.%, one additional time constant could be resolved for scans measured at exposure times ≥20 min.

Two modifications of the equivalent electrical circuit (EEC) were used for numerical simulation of electrode / solution interfaces, which are depicted in Fig. 5 (a for Nb concentrations from 4 to 32 at.% and b for Mg-44Nb). The systems can be modeled by ladder-type EECs, which consist of (R_iC_i) sub-circuits in series with R_Ω: R_i is electrical resistance, C_i is capacitance of the corresponding layer and R_Ω is resistance of the solution layer between the Luggin capillary and the working electrode. In the EECs in Fig. 5, the superposition of both porous layers (the underlying barrier MgO film and the uppermost one formed by corrosion products of Mg-*x*Nb alloy) was taken into account. In the EEC in Fig. 5a the electrolyte resistance across the $Mg(OH)_2$ film and its capacitance are represented by R_f and C_f, respectively. The parallel combination of R_{por} and the constant phase element (CPE_{por}) represent an inner barrier layer and the pair of R_{ct} and C_{ct} is attributed to the charge transfer process. The inductance L represents the impedance induced at low frequencies by adsorption processes, the influence of intermediates, composition non-homogeneity etc. [52–54]. In our case it occurred for immersion times ≥20 min. The general formula of this EEC is represented as $R_\Omega(R_f(C_f(CPE_{por}(R_{por}(C_{ct}(R_{ct}L))))))$. In accordance with the EEC arrangement, R_{ct}, R_{por} and R_f affected the corrosion process and their sum corresponds to the polarization resistance R_p of the electrode. In the case of Mg-44Nb alloy, the EEC depicted in Fig. 5b was the most consistent with experimental data sets. The formula of this EEC is $R_\Omega(R_f(C_f(C_{por}(R_{por}(CPE_{ct}R_{ct})))))$. In this EEC the CPE_{ct} parameter was applied instead of C_{ct}. The CPE parameter is usually introduced in EEC instead of pure *C* in order to take into account surface roughness, non-homogeneity of coating's composition, reactivity and a possible diffusion factor [54]. The impedance of *CPE* element Z_{CPE} is expressed by the equation:

$$Z_{CPE} = 1/[Y_0 \times (i\omega)^n], \quad (6)$$

where Y_0 is the electrode admittance, *i* is the imaginary unit ($\sqrt{-1}$), $\omega = 2\pi f$ is the angular frequency of the potential sine wave (rad · s^{-1}), *f* is the frequency in Hz; the value of n ranges between 0 and 1. The values 0, 0.5 and 1 of n imply that CPE of the EEC behaves as a pure resistor, diffusion impedance (W) and a capacitor, respectively. The used EECs gave the most satisfactory fitting, i. e. it was characterized by the lowest values of "chi square" parameter (χ^2) and weighted average error (as weighting factor impedance modules were used). Attempts to change (*W* instead of *L*, for example) or include more components into EEC resulted in unrealistically large errors for the new elements and reduced the quality of fitting significantly. The calculated values of EEC elements are summarized in Tables 1–6. In the cases where the exponent n was close to 1, the *CPE* values were treated as capacitances. It can be noted that n should be >0.75 in order to have reasonable confidence in *C* values [54, 55].

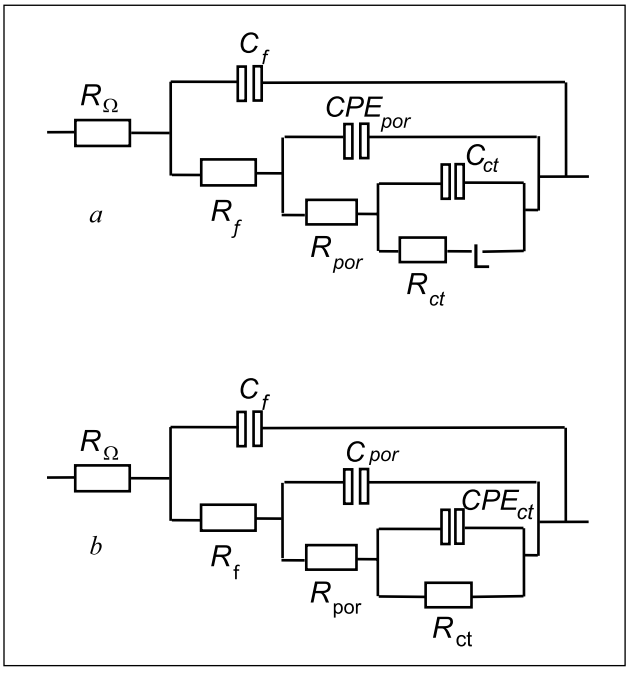

Fig. 5. Graphical schemes of equivalent electrical circuits used for simulation of EIS spectra of Mg-*x*Nb alloys: Mg-(4–32)Nb (*a*), Mg-44Nb (*b*)

The EIS fitted data provide more insight into the character of changes occurring during corrosion of Mg-*x*Nb alloys. Mg-4Nb alloy had the lowest values of parameters R_{ct} and R_{por} that characterize both the initial and developed corrosion resistance of appropriate electrodes: i. e. the sum of R_{ct} and R_{por} mainly determines the polarization resistance R_p. Thus, the values of R_{ct} and R_{por} after 5 min immersion of the studied alloys were the following: ~146.3 and ~129.5 Ω cm^{-2} for Mg-4Nb, ~921.5 and ~213.0 Ω cm^{-2} for Mg-9Nb, ~954.8 and ~251.6 Ω cm^{-2} for Mg-14Nb, ~5 689 and ~764.2 Ω cm^{-2} for Mg-26Nb, ~6 699 and ~702.7 Ω cm^{-2} for Mg-32Nb, ~6 830 and ~215.1 Ω cm^{-2} for Mg-44Nb (Tables 1–6). The increase in Nb concentration led to the increase of both parameters and also to larger difference in the values of R_{ct} and R_{por}. At the same time, for Mg-32Nb and Mg-44Nb alloys, which crystallized in the Nb *bcc* lattice, lower values of R_{por} were determined compared to the alloys which crystallized in the Mg *hcp* lattice. Especially significant decrease of R_{por} was determined for Mg-44Nb alloy: R_{por} was ~215.1 Ω cm^{-2} which is comparable with R_{por} ~213.0 Ω cm^{-2} found for Mg-9Nb. So, it can be concluded that both composition and structure (*hcp* or *bcc* in our case) determine the properties of a protective oxide layer.

The increase of immersion time from 5 min to 1 h led to a considerable increase of R_{ct} of all electrodes: e. g. from ~146.3 to ~2 380 Ω cm^{-2} for Mg-4Nb and from ~6 830 to

~13 034 Ω cm^{-2} for Mg-44Nb. For R_{por} another tendency was ascertained: the parameter increased moderately during 20 and 40 min of exposure in the Hank's solution, whereas at continued exposures the decrease or stabilization of R_{por} was observed. The character of changes of the corresponding values of C_{ct} and C_{por} (CPE_{por}) with immersion time also depended on alloy composition. Thus for the alloy with the lowest Nb content (Mg-4Nb) the decrease of both parameters after 1 h exposure was the most considerable: from ~25.0×10^{-5} to ~3.2×10^{-5} F cm^{-2} for C_{ct} and from ~8.68×10^{-5} to 0.14×10^{-5} F cm^{-2} for C_{por} (Table 1). Assuming the certain stability of dielectric constant of the barrier layer, significant reduction of both parameters was, most probably, determined by the increase of layer thickness due to the increase of pH at the interface, i. e. formation of $Mg(OH)_2$ according to reaction (2) and respective growth of MgO layer thickness according to equilibrium (4). The increase of Nb content in alloys led to changes of the above regularities. For Mg-9Nb alloy, C_{ct} changed inconsiderably during all exposure times and CPE_{por} increased from ~14.0×10^{-5} to 32.6×10^{-5} $S\ s^n$ cm^{-2} (Table 2). As known, *CPE* changes are indicative of interface condition changes: composition, thickness, current distribution and so on [54]. Though the confident values of C_{por} could not be precisely evaluated due to n < 0.75, it can be reliably concluded that the thickness of MgO layer did not increase significantly when the electrode was exposed to BSS from 20 to 60 min. It is mostly probable that changes of the interface composition (e. g. the enrichment of layer with Nb) had greater influence on the layer parameters CPE_{por} and R_{por}. For higher contents of Nb (14 and 26 at.%), the same tendency of C_{ct} and CPE_{por} increase with exposure time can be noted, which can also be attributed to changes in MgO layer thickness and composition (Table 3 and 4). At the same time

Table 1. $R_\Omega(C_f(R_f(CPE_{por}(R_{por}(C_{ct}(R_{ct}L))))))$ equivalent circuit data for Mg-4Nb electrodes in Hank's solution on immersion time

t, min	R_Ω, Ω cm^2	C_f, F cm^{-2}	R_f, Ω cm^2	CPE_{por}, Ss^n cm^{-2}; (n)	C_{por}, F cm^{-2}	R_{por}, Ω cm^2	R_{ct}, Ω cm^2	C_{ct}, F cm^{-2}	$\chi^2(Z_{err})$
5	28.0	6.3×10^{-6}	21.1	–	8.68×10^{-5}	129.5	146.3	25.0×10^{-5}	7.14×10^{-4} (<2.674)
20	31.6	4.7×10^{-5}	23.6	–	9.27×10^{-5}	206.5	461.6	16.9×10^{-5}	1.61×10^{-3} (<4.017)
40	32.7	6.8×10^{-6}	5.4	30.5×10^{-5} (0.77)	–	184.1	1 530	3.3×10^{-5}	1.25×10^{-4} (<1.12)
60	35.3	3.9×10^{-6}	8.6	28.1×10^{-5} (0.76)	–	178.7	2 202	3.2×10^{-5}	3.11×10^{-4} (<1.763)

Table 2. $R_\Omega(C_f(R_f(CPE_{por}(R_{por}(C_{ct}(R_{ct}L))))))$ equivalent circuit data for Mg-9Nb electrodes in Hank's solution on immersion time

t, min	R_Ω, Ω cm^2	C_f, F cm^{-2}	R_f, Ω cm^2	CPE_{por}, Ss^n cm^{-2}; (n)	R_{por}, Ω cm^2	R_{ct}, Ω cm^2	C_{ct}, F cm^{-2}	L, H cm^2	$\chi^2(Z_{err})$
5	35.6	4.7×10^{-6}	10.4	0.00014 (0.80)	213.0	921.5	2.3×10^{-5}	–	5.31×10^{-4} (<2.31)
20	35.6	1.50×10^{-6}	22.9	0.000281 (0.63)	200.7	3 192	2.3×10^{-5}	1 812	3.38×10^{-4} (<1.84)
40	36.3	1.8×10^{-6}	25.6	0.000256 (0.63)	302.0	4 274	2.4×10^{-5}	3 574	3.38×10^{-4} (<1.84)
60	36.5	1.8×10^{-6}	22.4	0.000326 (0.62)	331.6	3 905	2.7×10^{-5}	3 478	6.54×10^{-4} (<2.55)

Table 3. $R_\Omega(C_f(R_f(CPE_{por}(R_{por}(C_{ct}(R_{ct}L))))))$ equivalent circuit data for thin film Mg-14Nb electrodes in Hank's solution on immersion time

t, min	R_Ω, Ω cm^2	C_f, F cm^{-2}	R_f, Ω cm^2	CPE_{por}, Ss^n cm^{-2}; (n)	C_{por}, F cm^{-2}	R_{por}, Ω cm^2	R_{ct}, Ω cm^2	C_{ct}, Fcm^{-2}	L, H cm^2	$\chi^2(Z_{err})$
5	30.1	7.4×10^{-6}	17.9	0.000138 (0.77)		251.6	954.8	2.89×10^{-5}	–	4.83×10^{-4} (<2.22)
20	30.0	4.1×10^{-6}	15.7	0.000305 (0.62)		147.6	2 054	2.26×10^{-5}	1 249	1.85×10^{-4} (<1.36)
40	30.6	3.2×10^{-6}	21.0	0.000274 (0.64)		116	3 916	4.11×10^{-5}	3 930	3.48×10^{-4} (<1.87)
60	31.1	3.7×10^{-6}	19.2	0.000290 (0.64)		123.8	3 563	4.75×10^{-5}	4 492	3.90×10^{-4} (<1.99)

Table 4. $R_\Omega(C_f(R_f(CPE_{por}(R_{por}(C_{ct}(R_{ct}L))))))$ equivalent circuit data for Mg-26Nb electrodes in Hank's solution on immersion time

t, min	R_Ω, Ω cm^2	C_f, F cm^{-2}	R_f, Ω cm^2	CPE_{por}, Ss^n cm^{-2}; (n)	R_{por}, Ω cm^2	R_{ct}, Ω cm^2	C_{ct}, F cm^{-2}	L, H cm^2	$\chi^2(Z_{err})$
5	31.1	5.4×10^{-6}	18.6	4.5×10^{-5} (0.82)	764.2	5 689	3.75×10^{-6}	–	1.59×10^{-4} (<1.26)
20	31.6	5.8×10^{-6}	23.5	5.4×10^{-5} (0.81)	861	6 953	6.72×10^{-6}	–	2.73×10^{-4} (<1.67)
40	31.5	6.24×10^{-6}	26.6	6.7×10^{-5} (0.80)	853.7	7 655	9.99×10^{-6}	–	8.14×10^{-4} (<2.85)
60	31.4	5.01×10^{-6}	24.1	9.3×10^{-5} (0.75)	599.6	7 820	1.02×10^{-5}	–	6.4×10^{-4} (<2.53)

it should be emphasized that the discussed regularities were not monotonic: some fluctuations (i. e. alteration of increase / decrease stages) were characteristic of all alloys investigated. For the alloys with 32 and 44 at.% of Nb, strict regularities of the changes of C_{ct} (or CPE_b) and CPE_{por} (or C_{por}) were not determined (Tables 5 and 6) as well. For Mg-32Nb alloy, the initial decrease of C_{ct} from ~4.96×10^{-5} at 5 min exposure to ~1.28×10^{-5} F cm^{-2} at 40 min exposure was followed by further increase up to ~1.69×10^{-5} F cm^{-2} (Table 5). For Mg-44Nb alloy, an analogous "oscillations" of CPE_b can be noted. Parameters CPE_{por} and C_{por} of the respective alloys also were not stable: CPE_{por} of Mg-32Nb alloy increased from ~4.22×10^{-5} to ~23.0×10^{-5} S s^n cm^{-2} during 1 h exposure, whereas C_{por} decreased from ~1.23×10^{-5} to ~0.67×10^{-5} F cm^{-2} during the same immersion time. Similarly to the cases of other alloys, it is most probable that these regularities were determined first of all by changes in the composition of the layers. The "oscillations" of CPE_{por} and C_{por} values during exposure were characteristic of these alloys as well.

Parameters R_f and C_f characterized the outer layer of corrosion products formed on the surface of Mg-*x*Nb alloys. $Mg(OH)_2$ is the basic component of this layer. Initial values of R_f ranged from the maximum value of ~23.9 Ω cm^2 for Mg-32Nb to the lowest one ~10.4 Ω cm^2 for Mg-9Nb. The increase in R_f values during the first immersion stages, followed by a slight decrease, was determined for most of the alloys. The lowest value of R_f was determined for Mg-4Nb alloy: ~5.4 Ω cm^2 after 40 min exposure (Table 1). The initial value of R_f for Mg-44Nb alloy was ~40.6 Ω cm^2 (Table 6). During the first stages of exposure it increased till ~108.3 Ω cm^2 and afterwards slightly decreased to ~98.6 Ω cm^2. Initial values of C_f for alloys with the Nb content ranging from 4 to 26 at.% were determined to be of the order of few microfarads. As can be seen, these values were considerably less than the corresponding C_{por} ones. Thus, it means that the outer layer of corrosion products was considerably thicker than the inner one. The thickness (d) of the outer layer of corrosion products could be roughly estimated according to the formula for plain capacitor [52]:

$$C_f = \varepsilon\varepsilon_0 S/d, \quad (7)$$

where S is the surface area, $S = 1$ cm^2, $\varepsilon_0 = 8.85 \times 10^{-14}$ F cm^{-1} is the vacuum permittivity and $\varepsilon \approx 80$ is the assumed relative dielectric constant of magnesium hydroxide in chloride-containing electrolytes [56]. For Mg-4Nb alloy the fitted value of C_f is ~ 6.3×10^{-6} F cm^{-2}. Hence, the layer should be ~11.2 nm thick. For Mg-32Nb and Mg-44Nb alloys the calculated values of C_f were higher: ~$(1.1–2.3) \times 10^{-5}$ F cm^{-2}, i. e. they should be coated with thinner outer layers. However, the relative dielectric constant of niobium oxide varies in the wide range, from ~30 to ~120 [57], therefore, the composition of layers should be known for the exact evaluation of (d). The considerable variation of C_f during exposure in the Hank's solution can also be mentioned: periods of monotonic increase of the parameter were followed by its reduction.

The values of R_Ω in Tables 1–6 varied in the range from ~25 to ~40 Ω cm^2. The real R_Ω values for the electrolytes with the used concentrations of components should be considerably less, i. e. ~2 Ω cm^2 [58]. It is most likely that during the simulation of experimental spectra the fitted R_Ω values were influenced by the simulated parameters of the outer layer of corrosion products [54]. However, attempts to include additional (RC)-subcircuit into EECs or to strictly separate (R_fC_f)-subcircuit from $R_\times$ produced unrealistically large errors of simulation. It can be concluded that the used EECs are not precisely adequate for the studied systems.

Table 5. $R_\Omega(C_f(R_f(CPE_{por}(R_{por}(C_{ct}(R_{ct}L))))))$ equivalent circuit data for Mg-32Nb electrodes in Hank's solution on immersion time

t, min	R_Ω, Ω cm^2	C_f, F cm^{-2}	R_f, Ω cm^2	CPE_{por}, Ss^n cm^{-2}; (n)	C_{por}, F cm^{-2}	R_{por}, Ω cm^2	R_{ct}, Ω cm^2	C_{ct}, F cm^{-2}	L, H cm^2	χ^2 ($<Z_{err}$)
5	27.6	1.1×10^{-5}	23.9	4.2×10^{-5} (0.81)		702.7	3 699	4.96×10^{-5}	–bl.	9.68×10^{-5} (<0.98)
20	27.3	1.4×10^{-5}	14.9	11.6×10^{-5} (0.70)		639.2	4 273	7.52×10^{-6}	3 687	1.57×10^{-4} (<1.25)
40	27.3	1.2×10^{-5}	13.2	18.9×10^{-5} (0.67)		726.7	4 492	1.28×10^{-5}	9 037	1.05×10^{-4} (<1.03)
60	27.4	1.0×10^{-5}	13.6	23.0×10^{-5} (0.63)		751.2	4 349	1.69×10^{-5}	13 700	1.73×10^{-4} (<1.32)

Table 6. $R_\Omega(C_f(R_f(C_{por}(R_{por}(CPE_{ct}R_{ct})))))$ equivalent circuit data for Mg-44Nb electrodes in Hank's solution on immersion time

t, min	R_Ω, Ω cm^2	C_f, F cm^{-2}	R_f, Ω cm^2	C_{por}, F cm^{-2}	R_{por}, Ω cm^2	R_{ct}, Ω cm^{2z}	CPE_{ct}, Ss^n cm^{-2}; (n)	χ^2 ($<Z_{err}$)
5	32.4	2.3×10^{-5}	40.6	1.2×10^{-5}	215.1	6 830	4.05×10^{-5} (0.75)	1.74×10^{-4} (<1.32%)
20	32.1	2.3×10^{-5}	108.3	1.0×10^{-5}	679.2	12 780	3.21×10^{-5} (0.79)	9.9×10^{-4} (<3.16%)
40	31.8	2.0×10^{-5}	97.7	8.7×10^{-6}	638.9	12 330	3.53×10^{-5} (0.79)	2.47×10^{-4} (<1.52%)
60	34.0	1.8×10^{-5}	98.6	7.5×10^{-6}	694.2	12 340	3.26×10^{-5} (0.78)	2.1×10^{-4} (<1.47%)

CONCLUSIONS

Mg-*x*Nb alloys with Nb content ranging between 4 and 44 at.% were formed by DC magnetron sputtering. Corrosion resistance of the alloys was studied in Hank's solution with the aim to predict the corrosion behaviour for in vivo applications. Solution analysis, DC voltammetry, XPS and EIS measurements showed ennoblement of the alloys with increase in Nb concentration and high corrosion resistance when the Nb content exceeded ~26 at.%. EIS data indicated the presence of two oxygen containing layers on the corroding surface: a thin highly protective but porous one adjacent to the metal and a thick but poorly protective one on the top. It was suggested that corrosion reactions occur predominantly within the pores of the protective thin layer. The investigations show that the corrosion process of Mg-Nb alloys could be controlled by changing Nb content to adjust the corrosion rate according to biomedical in vivo needs.

ACKNOWLEDGEMENTS

The study has been supported by the Research Council of Lithuania (Contract MIP-119/2012).

Received 5 December 2014
Accepted 22 December 2014

References

1. C. MacChi, C. Maurizio, R. Checchetto, et al., *Phys. Rev. B: Condens. Matter Mater. Phys.*, **85(21)**, 214117 (2012).
2. P. Mengucci, G. Barucca, G. Majni, N. Bazzanella, R. Checchetto, A. Miotello, *J. Alloys Compd.*, **509(2)**, S572 (2011).
3. M. Shanthi, P. Jayaramanavar, V. Vyas, D. V. S. Seenivasan, M. Gupta, *J. Alloy Compd.*, **513**, 202 (2012).
4. B. Ham, X. Zhang, *Mat. Sci. Eng.*, A **528(4–5)**, 2028 (2011).
5. L. Toniutti, R. Checchetto, P. Mengucci, A. Miotello, R. S. Brusa, *Phys. Status Solidi C*, **6(11)**, 2310 (2009).
6. P. Mosaner, N. Bazzanella, M. Bonelli, M. Checchetto, A. Miotello, *Mater. Sci. Eng., B*, **108(1–2)**, 33 (2004).
7. J. F. R. De Castro, A. L. M. Costa, S. F. Santos, W. J. F. Botta, T. T. Ishikawa, A. R. Yavari, *J. Metastab. Nanocryst.*, **20–21**, 349 (2004).
8. C. X. Shang, M. Bououdina, Z. X. Guo, *J. Alloys Compd.*, **349(1–2)**, 217 (2003).
9. K. Klyukin, M. G. Shelyapina, D. Fruchart, *Solid State Phenom.*, **170**, 298 (2011).
10. S. Bao, Y. Yamada, K. Tajima, M. Okada, K. Yoshimura, *Jpn. J. Appl. Phys.*, **46**, L13 (2007).
11. S. Bao, K. Tajima, Y. Yamada, P. Jin, M. Okada, K. Yoshimura, *Jpn. J. Cer. Soc.*, **116(6)**, 771 (2008).
12. B. Heublein, R. Rohde, V. Kaese, M. Niemeyer, W. Hartung, A. Haverich, *Heart*, **89**, 651 (2003).
13. E. Hirota, H. Habazaki, A. Kawashima, K. Asami, K. Hashimoto, *Sci. Rep. Res. Tohoku*, **A38**, 53 (1993).
14. F. Witte, V. Kaese, H. Haferkamp, et al., *Biomaterials*, **26**, 3557 (2005).
15. M. P. Staiger, A. M. Pietak, J. Huadmai, G. Dias, *Biomaterials*, **27**, 1728 (2006).
16. F. Witte, *Acta Biomater.*, **6**, 1680 (2010).
17. M. Alvarez-Lopez, M. D. Pereda, J. A. del Valle, et al., *Acta Biomater.*, **6**, 1763 (2010).
18. N. T. Kirkland, J. Lespagnol, N. Birbilis, M. P. Staiger, *Corros. Sci.*, **52**, 287 (2010).
19. H. Hermawan, D. Dubé, D. Mantovani, *Acta Biomater.*, **6**, 1693 (2010).
20. N. Hort, Y. Huang, D. Fechner, et al., *Acta Biomater.*, **6**, 1714 (2010).
21. A. Purnama, H. Hermawan, J. Couet, D. Mantovani, *Acta Biomater.*, **6**, 1800 (2010).
22. H. Hornberger, S. Virtanen, A. R. Boccaccini, *Acta Biomater.*, **8**, 2442 (2012).
23. A. Hartwig, *Mutat Res.*, **475**, 113 (2001).
24. Y. H. Yun, Z. Dong, D. Yang, et al., *Mat. Sci. Eng. C.*, **29**, 1814 (2009).
25. L. Kouisni, M. Azzi, M. Zertoubi, F. Dalard, S. Maximovitch, *Surf. Coat. Tech.*, **185**, 58 (2004).
26. M. M. El-Omar, G. Dangas, I. Iakovou, R. Mehran, *Curr. Interv. Cardiol. Rep.*, **3**, 296 (2001).
27. V. T. Kaesel, P. T. Tai, F. W. Bach, H. Haferkamp, F. Witte, H. Windhagen, *Proceedings of the Sixth International Conference: Magnesium Alloys and Their Applications*, Wiley VCH, New York (2004).
28. N. Hort, Y. Huang, D. Fechner, et al. *Acta Biomater.*, **6**, 1714 (2010).
29. G. Song, *Corr. Sci.*, **49**, 1696 (2007).
30. N. C. Quach, P. J. Uggowitzer, P. Schmutz, *C. R. Chim.*, **11**, 1043 (2008).
31. A. C. Hanzi, P. Gunde, M. Schinhammer, P. J. Uggowitzer, *Acta Biomater.*, **5**, 162 (2009).
32. M. Liu, P. Schmutz, P. J. Uggowitzer, G. Song, A. Atrens, *Corr. Sci.*, **52**, 3687 (2010).
33. A. C. Hanzi, I. Gerber, M. Schinhammer, J. F. Löffler, P. J. Uggowitzer, *Acta Biomater.*, **6**, 1824 (2010).
34. P. Gunde, A. C. Hänza, A. S. Sologubenko, P. J. Uggowitzer, *Mater. Sci. Eng. A*, **528**, 1047 (2011).
35. T. Kraus, S. F. Fischerauer, A. C. Hanzi, P. J. Uggowitzer, J. F. Löffler, A. M. Weinberg, *Acta Biomater.*, **8**, 1230 (2012).
36. H. Wang, Y. Estrin, Z. Zuberova, *Mater Lett.*, **62**, 2476 (2008).
37. L. Li, J. Gao, Y. Wang, *Surf. Coat. Technol.*, **185**, 92 (2004).
38. Y. Wang, M. Wei, J. Gao, *Mater. Sci. Eng. C*, **29(4)**, 1311 (2009).
39. Y. Song, S. Zhang, J. Li, C. Zhao, X. Zhang, *Acta Biomater.*, **6**, 1736 (2010).
40. C. K. Yuen, W. Y. Ip, *Acta Biomater.*, **6**, 1808 (2010).
41. Z. Li, X. Gu, S. Lou, Y. Zheng, *Biomater.*, **29**, 1329 (2008).
42. T. D. Lucey, B. Venugopal, *Metal Toxicity in Mammals*, Plenum Press, New York (1977).
43. J. Crossgrove, W. Zheng, *NMR Biomed.*, **17**, 544 (2004).
44. A. A. Nayeb-Hashemi, J. B. Clark, *Phase Diagrams of Binary Magnesium Alloys*, ASM International, Materials Park, OH (1988).

45. H. K. Westengen, in: K. H. Jurgen, R. W. Cahn, M. C. Flemings, B. Ilschner, E. J. Kramer, S. Mahajan (eds.), *Encyclopedia of Materials: Science and Technology*, Elsevier Science Ltd. (2001).
46. R. Godley, D. Starosvetsky, I. Gotman, *J. Mater. Sci.-Mater. M.*, **15(10)**, 1073 (2004).
47. V. V. Starikov, S. L. Starikova, A. G. Mamalis, S. N. Lavrynenko, J. J. Ramsden, *J. Biol. Phys. Chem.*, **7(4)**, 141 (2007).
48. C. D. Wagner, A. V. Naumkin, A. Kraut-Vass, J. W. Allison, C. J. Powell, J. R. Rumble, *NIST Standard Reference Database 20, Version 3.4 (Web Version)* (2007).
49. A. Grigucevičienė, L. Staišiūnas, P. Miečinskas, R. Giraitis, K. Leinartas, E. Juzeliūnas, *Chemija*, **24(3)**, 190 (2013).
50. M. Pourbaix, *Atlas of Electrochemical Equilibria in Aqueous Solutions*, Pergamon Press, Elmsford, NY (1966).
51. P. Agarwal, M. E. Orazem, L. H. Garcia-Rubio, *J. Electrochem. Soc.*, **139**, 1917 (1992).
52. G. Baril, G. Galicia, C. Deslouis, N. Pébère, B. Tribollet, V. Vivier, *J. Electrochem. Soc.*, **154(2)**, C108 (2007).
53. J. Chen, J. Wang, E. Han, J. Dong, W. Ke, *Electrochim. Acta*, **52**, 3299 (2007).
54. M. Orazem, B. Tribollet, *Electrochemical Impedance Spectroscopy*, John Wiley & Sons, Inc., New Jersey (2008).
55. C. S. Hsu, F. Mansfeld, *Corrosion*, **57(9)**, 747 (2001).
56. P. Wang, A. Anderko, *Fluid Phase Equilib.*, **186**, 103 (2001).
57. A. Michaelis, in: R. C. Alkire, D. M. Kolb, J. Lipkowski, P. N. Ross (eds.), *Advances in Electrochemical Science and Engineering*, Vol. 10, Wiley VCH, Weinheim (2008).
58. K. Leinartas, D. Bražinskienė, P. Miečinskas, et al., *T. I. Met. Finish.*, **91(4)**, 182 (2013).

Asta Grigucevičienė, Konstantinas Leinartas, Laurynas Staišiūnas, Povilas Miečinskas, Vitalija Jasulaitienė, Jūratė Vaičiūnienė, Eimutis Juzeliūnas

PLONŲ Mg-Nb LYDINIŲ SLUOKSNIŲ KOROZINIS ATSPARUMAS HANK'O BALANSINIAME DRUSKŲ TIRPALE

S a n t r a u k a

Mg-Nb lydiniai su Nb koncentracija nuo 4 iki 44 at.% buvo suformuoti magnetroninio dulkinimo metodu. Lydinių elektrocheminė ir korozinė elgsena tirta Hank'o balansiniame druskų tirpale optinės emisijos spektroskopijos (OES), voltamperometrijos, elektrocheminio impedanso spektroskopijos (EIS) ir rentgeno fotoelektroninės spektroskopijos (RFS) metodais. Tyrimais nustatyta, kad didėjant Nb koncentracijai lydinyje didėja jo inertiškumas. Didžiausias korozinis atsparumas nustatytas, kai Nb koncentracija lydinyje viršija ~26 at.%. Remiantis EIS duomenų analize galima teigti, kad koroduojančio lydinio paviršiuje formuojasi du oksidiniai sluoksniai: arčiau metalo – plonas, pasižymintis didele apsaugine geba, ir išorinis – storesnis, bet poringas ir mažiau pasyvus. Padaryta išvada, kad korozijos reakcijos paprastai vyksta plono apsauginio sluoksnio, sudaryto iš MgO + NbO, porose. Keičiant Nb koncentraciją Mg-Nb lydiniai gali būti pritaikyti biomedicinos poreikiams.